

KODAIKANAL CALCIUM IMAGES: DETECTION OF PLAGES, FIXING THE HELIOGRAPHIC COORDINATES AND ESTIMATION OF AREA

K. M. Hiremath^{1,2}, Shreyam Krishna³, Adithya H. N⁴, S. R. Chinmaya⁵ and Shashanka R Gurumath⁶

1. Formerly Indian Institute of Astrophysics, Bangalore, India Email: hiremath@iiap.res.in
2. #23, Mathru Pithru Krupa, 2nd Cross, 1st Main, BDA Layout, Bikasipura, BSK V Stage, Bengaluru-560111, India
3. B-9, Sector H, Aliganj Near Sangam Crossing Lucknow, Uttar Pradesh, India
4. #76, Neelanduru Nalluru, Sringeri, Chikkamagaluru, Karnataka, India
5. #3, First floor, 12th Main road, Lakkasandra extension. Bangalore 560030, India
6. Physical Research Laboratory, Navrangpura, Ahmedabad - 380009, India

ABSTRACT

Kodaikanal Observatory is a veritable treasure trove of data, with the data repository covering almost 100 years of observations. For the years 1909-2007, we use calibrated Ca II K spectroheliograms from the Kodaikanal Observatory to detect the plagues, fix their heliographic coordinates and also estimate the plague areas. We adopt the following procedure. After ensuring that, for all the years, Kodai calcium images have very negligible ellipticity, a circle is fitted and two central coordinates and radius of calcium images are determined uniquely. For each pixel of the calcium image, we then fix heliographic coordinates and extract plagues along with their weighted average coordinates. The heliographic coordinates of these extracted plagues are then compared with the heliographic coordinates of photospheric sunspots from the Greenwich sunspot database and chromospheric magnetic plagues detected from the SOHO/MDI magnetograms. We find that the heliographic coordinates of calcium plagues match very well with the heliographic coordinates of sunspots and magnetic plagues authenticating our method of detection of plagues and computation of positional coordinates. A code is developed in Python and all the nearly century scale plagues data, with accurately estimated heliographic coordinates and areas, is available to the public.

1 INTRODUCTION

Two unsolved mysteries of the sun are genesis of solar cycle and activity phenomena and how sun's irradiance varies with the short and long term time scales. Although so called flux transport dynamo models apparently reproduce butterfly diagram, question remains how to reproduce the integrated solar cycle and activity phenomena such as sunspots, coronal holes, faculae, plagues, *etc.* Other important and pertinent question is whether solar cycle and activity phenomena can be understood from the flux transport dynamo models or superposition of long period (~ 11 yrs or more) MHD waves that probably might have generated and might have traveled along the fossil magnetic field structure (Alfvén 1943, Hiremath 1994, Hiremath 1995). Infact, from the century scale sunspot

data of the Greenwich photoheliographic results, Gokhale *et.al.* (1990) came to the conclusion that sunspots might have originated from the superposition of long period MHD waves. Hiremath (2010) showed that well known solar periods can be reproduced from the perturbation of combined poloidal and toroidal magnetic field structure embedded in the sun's interior, probably of primordial origin.

For validation of both the turbulent dynamo and MHD oscillation models and to test which model is most consistent and appropriate to explain the combined solar cycle and activity phenomena, observational information regarding sun's long term (≥ 10 yrs) magnetic activity is required. Although magnetic activity information inferred from the magnetograms is nearly five decades old, sun's activity on century scale that may yield clues regarding mystery of Maunder minimum type of activity warrants nearly century scale or greater than time scale of magnetogram data.

Recent overwhelming evidences (Hiremath 2009, Hiremath 2015) are building up that influence of sun's activity phenomena on the Earth's climate can not be neglected so easily. If we understand this sun-Earth climate relationship, we can also understand the stars-planets climate relationship and ultimately to search for habitable exoplanets in the universe. Hence, for deep understanding of sun-Earth's climate relationship, information regarding long-term variation of solar irradiance is required.

Considering the importance of long-term variations of sun's magnetic and irradiance activities, Kodaikanal calcium data is ideally suited. In Kodaikanal, we have a treasure trove of both the white light and calcium image data observed from the same relevant instruments with very good seeing conditions. As there is one to one correspondence between (Ortiz and Rast 2005, Sivaraman and Livingston 1982, Rodono *et.al.* 1987, Frasca *et.al.* 2000, Butler 1995, Frasca *et.al.* 2008, Loukitcheva *et.al.* 2009, Frasca *et.al.* 2010, Bertello *et.al.* 2016a, Bertello *et.al.* 2016b, Pevtsov *et.al.* 2016) calcium plages and photospheric magnetic activity, calcium plages can be used as proxy for understanding the long term variation of magnetic activity of the sun. As chromospheric activity is one of the main contributor for the solar irradiance, analysis and extraction of chromospheric activity parameters are very useful for modeling and reconstruction of long-term solar irradiance variations.

Aims of present study are to: i) uniquely estimate the center and radius of the calcium image, ii) reasonably detect boundary of the plages, iii) from *ab initio*, accurately fix the heliographic coordinates for all the pixels of the image and compute the average heliographic coordinates (such as latitude and longitude from the central meridian) of plages and, iv) as presented in the following sections, validate position (heliographic coordinates) of Kodai calcium plages with the position of photospheric magnetic sunspots and chromospheric magnetic plages and, v) validate the estimated projectional corrected calcium plage areas with the chromospheric magnetic plage areas.

From the extracted heliographic coordinates, in future, we plan to investigate the nature of latitudinal and long-term (\sim century scale) temporal variation of chromospheric rotation rate profile. Cycle to cycle variation and long-term changes in the velocity of meridional circulation (for which accurate estimation of heliographic coordinates is required) and its relationship with the photospheric and deep interior meridional circulation will also be

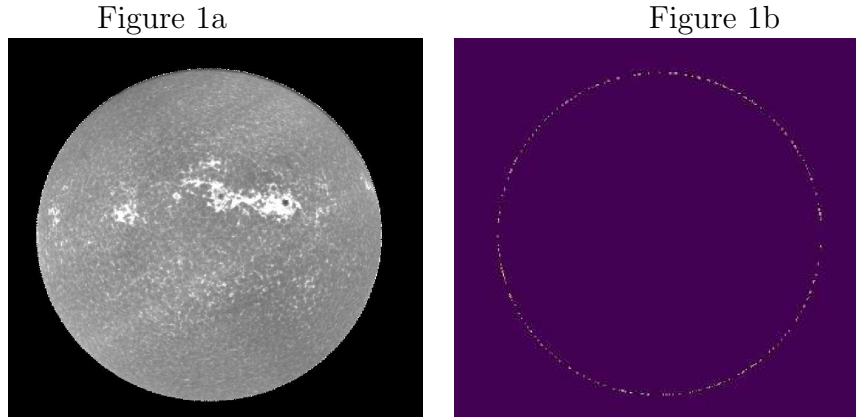


Figure 1: Figure 1a illustrates the calibrated Ca II K Spectroheliogram from the Kodaikanal Observatory data. Where as Figure 1b illustrates the detected edge of the solar image.

investigated.

Present study is not a first study to delineate the plages from the calcium images, fix the heliographic coordinates and estimate the areas. However, most of the previous studies (Foukal 1996, Balmaceda *et.al.* 2009, Ermolli *et.al.* 2009a, Ermolli *et.al.* 2009b, Tlatov *et.al.* 2009, Bertello *et.al.* 2010, Priyal *et.al.* 2014, Chatterjee *et.al.* 2016, Chatzistergos 2017, Priyal *et.al.* 2017, Chatzistergos *et.al.* 2018, Barata *et.al.* 2018) mainly concentrated on estimating hemispheric contribution of plage areas. Although some of these studies attempted to estimate the heliographic coordinates of the plages, clarity regarding method of estimation of heliographic coordinates and their accuracy is lacking. In addition, most of these studies do not apply the projectional corrections for the estimated areas of the plages. Present study fulfill both of these objectives.

Plan of the paper is as follows. In section 2, data and analysis of the Kodai calcium image data are presented. In section 3, the results are presented and, last section consists of the conclusions emerged from this study.

2 DATA AND ANALYSIS

The Kodaikanal Solar Observatory has been observing the Sun in the Ca II K line since 1905 by using photographic plates illuminated by 30 cm objective telescope. With a spatial resolution of about 2 arc sec, calcium narrow band filter is used to obtain the spectroheliograms in Ca II K line. This data repository spans over hundred years, from 1905 - 2007. Recently nearly century scale data of calcium images is digitized by 4096 x 4096 pixels, with a pixel size of 0.85 arc seconds. Details of the telescope, digitization and calibration can be found in the previous (Priyal *et.al.* 2014, Priyal *et.al.* 2017) studies. Typical calibrated calcium image is illustrated in Figure 1a.

2.1 Methods Of Analysis Of Solar Images

2.1.1 Edge Detection

The method we have used to find the radius and the center is solving three simultaneous equations that have three unknowns (two central coordinates and one radial coordinate). Hence by solving three equations with three unknowns, the center and the radius of circle are estimated uniquely. We consider every data point in the detected solar disk edge for least-square fitting. The added advantage is, we have taken all the pixels of the detected edge and circle is fitted for the sun, which is better estimation than taking a few data points as used in most of the previous studies.

The edge of the sun is detected using OpenCVs canny edge detection function which consists of 4 parts:

- a) 5x5 Gaussian filter is used for the removal of the noise in the images.
- b) Sobel filter is used to get vertical and horizontal gradients from smoothed image. From these two horizontal and vertical gradient images, edge gradient G and angle θ for each pixel are obtained by using the following formulae:

$$G = (G_x^2 + G_y^2)^{1/2}, \quad (1)$$

and

$$\theta = \tan^{-1}\left(\frac{G_y}{G_x}\right). \quad (2)$$

where G_x is the gradient in x direction and G_y is the gradient in y direction which are perpendicular to edges.

- c) In order to remove any unrelated pixels that are not part of the edge, each pixel is checked in the direction of the gradient to confirm that it is the local maximum in its neighborhood.

- d) First minimum and maximum intensity values of edges are estimated. Then any edge intensity greater than maximum intensity values are considered to be sure edges, otherwise are considered to be of non-edges. Whereas the edge intensities that lie between maximum and minimum intensity edge values are classified as either edges or no-edges depending on their connectivity. Connected edges are considered to be “sure-edge” pixels which are subset of edges, otherwise are discarded. This step is known as Hysteresis Thresholding.

Canny edge detection was chosen as the preferred method after comparing it with Sobel x, Sobel y and Laplacian edge detection methods. The comparison revealed that the error in detection of edge was lowest in canny edge detection. Following all these steps, detected edge of the calcium image is illustrated in Figure 1b.

2.1.2 Circle Fitting

All the detected pixels of edge of the image is least-square fitted with a circle that uses a system of simultaneous three equations with three unknowns to get a unique solution for center and radius of the solar image. This method only requires that the edge of the

circle coordinates be the input and initial guess is not required. This method computes uniquely the three required coordinates (two coordinates for center of the circle and the radius). The process is described in detail below:

If x_i and y_i (where $i = 1, N$, N is total number) are Cartesian coordinates of the detected pixels and, \bar{x} and \bar{y} are their respective means which are defined as follows

$$\bar{x} = \frac{\sum_i x_i}{N}, \quad (3)$$

and

$$\bar{y} = \frac{\sum_i y_i}{N}. \quad (4)$$

Let x_i and y_i be further transferred into new variables u_i, v_i such that

$$u_i = x_i - \bar{x}, \quad (5)$$

and

$$v_i = y_i - \bar{y}. \quad (6)$$

Let (u_c, v_c) be the center coordinates of the circle with radius R and $\alpha = R^2$.

Distance of any point (u_i, v_i) from the center is $[(u_i - u_c)^2 + (v_i - v_c)^2]^{1/2}$.

From the method of least-square fit which implies function $S = \sum_i [g(u_i, v_i)]^2$ should be minimum wherein

$$g(u_i, v_i) = (u_i - u_c)^2 + (v_i - v_c)^2 - \alpha. \quad (7)$$

Hence, partial derivatives of this function with respect to α, u_c and v_c should all be zero. For the partial derivative of S with respect to α we get

$$\frac{\partial S}{\partial \alpha} = 2 \sum_i g(u_i, v_i) \frac{\partial g}{\partial \alpha} = 0, \quad (8)$$

$$\Rightarrow -2 \sum_i g(u_i, v_i) = 0, \quad (9)$$

$$\Rightarrow \sum_i [(u_i - u_c)^2 + (v_i - v_c)^2 - \alpha] = 0, \quad (10)$$

$$\Rightarrow \sum_i u_i^2 + \sum_i v_i^2 + \sum_i u_c^2 + \sum_i v_c^2 - 2[\sum_i u_i u_c + \sum_i v_i v_c] = \sum_i \alpha, \quad (11)$$

$$\Rightarrow [\sum_i u_i^2 + \sum_i v_i^2] + N[u_c^2 + v_c^2] - 2[u_c \sum_i u_i + v_c \sum_i v_i] = N\alpha. \quad (12)$$

With a known fact that $\sum_i u_i = \sum_i (x_i - \bar{x}) = N\bar{x} - N\bar{x} = 0$ and, $\sum_i v_i = 0$, we get

$$\Rightarrow \sum_i u_i^2 + \sum_i v_i^2 + N[u_c^2 + v_c^2] = N\alpha. \quad (13)$$

For the partial derivative of S with respect to u_c we get

$$\frac{\partial S}{\partial u_c} = 2 \sum_i g(u_i, v_i) \frac{\partial g}{\partial u_c} = 0, \quad (14)$$

$$\Rightarrow \sum_i (u_i - u_c) g(u_i, v_i) = 0. \quad (15)$$

On expansion, we get

$$\Rightarrow \sum_i u_i^3 + \sum_i u_i v_i^2 - 2u_c \sum_i u_i^2 - 2v_c \sum_i u_i v_i - u_c \sum_i u_i^2 \quad (16)$$

$$-u_c \sum_i v_i^2 - Nu_c^3 - Nu_c v_c^2 + N\alpha u_c = 0 \quad (17)$$

By substituting the value $N\alpha$ from equation (13), we get

$$u_c \sum_i u_i^2 + v_c \sum_i u_i v_i = \frac{1}{2} [\sum_i u_i^3 + \sum_i u_i v_i^2] \quad (18)$$

Lastly partial derivative of S with respect to v_c yields the following equation

$$\frac{\partial S}{\partial v_c} = 2 \sum_i g[u_i, v_i] \frac{\partial g}{\partial v_c} = 0, \quad (19)$$

Following the derivations of above equations (8)-(13), we obtain the following equation:

$$u_c \sum_i u_i v_i + v_c \sum_i v_i^2 = \frac{1}{2} [\sum_i v_i^3 + \sum_i v_i u_i^2]. \quad (20)$$

Simultaneous solution of equations (18) and (20) yield the two central coordinates u_c and v_c . Then from equation (13), we get the value of α ($= R^2$) and, hence the radius R .

By adding two central coordinates (u_c, v_c) to the respective means, original central coordinates x_c and y_c are obtained

$$x_c = u_c + \bar{x}, \quad (21)$$

and

$$y_c = v_c + \bar{y}. \quad (22)$$

Hence, importance of this method is from the observed sun's image, two central coordinates and its radius are obtained uniquely.

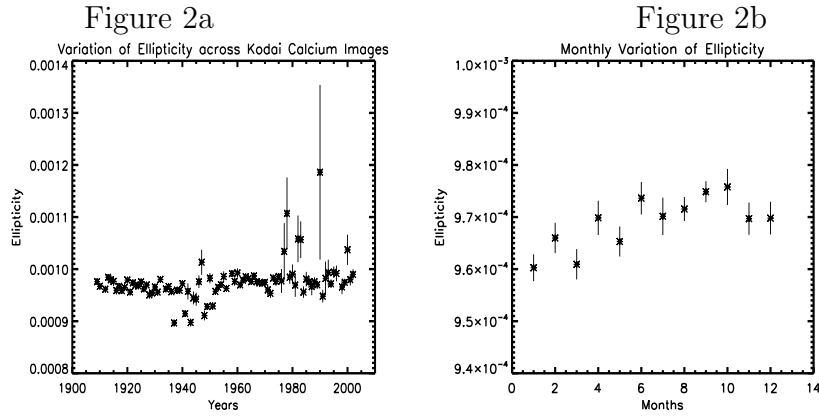


Figure 2: Figure 2a illustrates estimated annual ellipticity and whereas Figure 2b illustrates the same parameter for different months of a year.

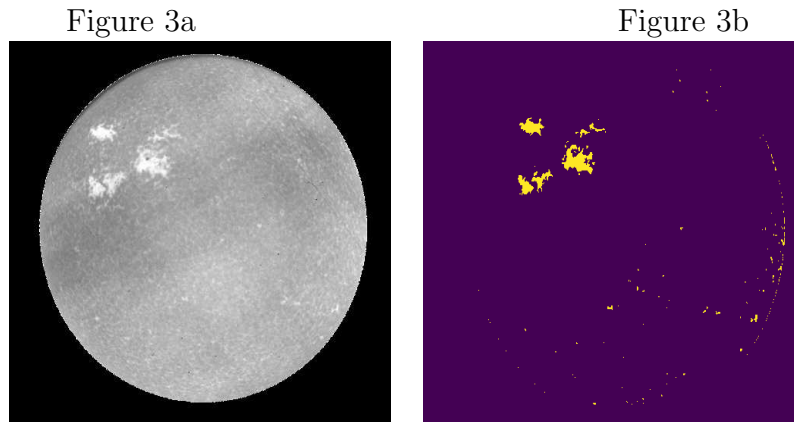


Figure 3: Figure 3a illustrates the original calcium image, whereas, Figure 3b illustrates the image with detected plages.

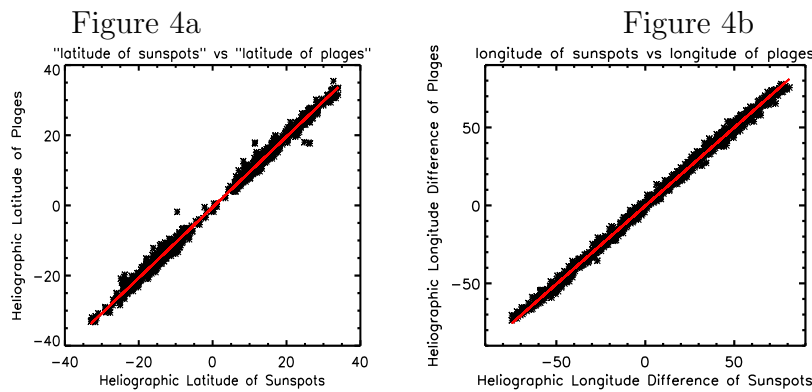


Figure 4: Figure 4a illustrates a scatter plot between estimated average latitude of calcium plage and sunspot latitude. Figure 4b illustrates a scatter plot between average longitude from the central meridian of a detected plage and the sunspot.

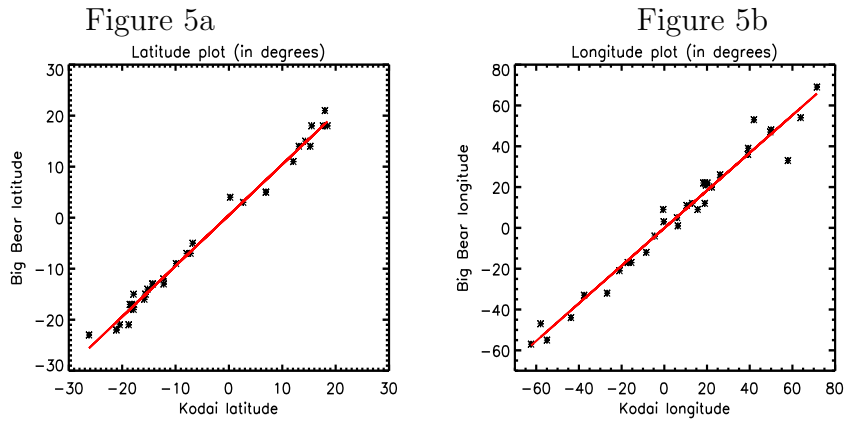


Figure 5: Figure 5a illustrates a scatter plot between estimated Kodai average latitude of calcium plage with the estimated Big Bear calcium plage latitude. Whereas 5(b) illustrates a scatter plot between estimated Kodai average longitude of calcium plage with the estimated Big Bear calcium plage longitude.

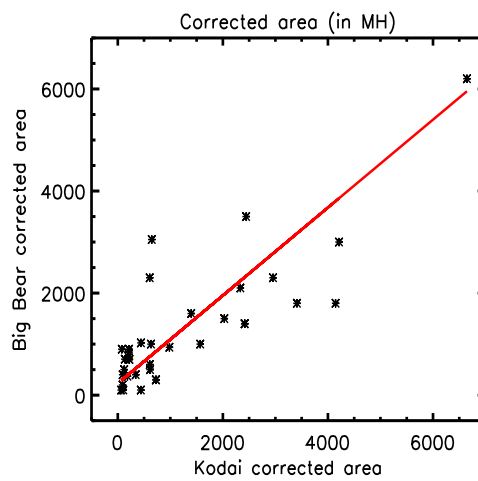


Figure 6: Illustrates a scatter plot between estimated average area (in mh) of Kodai calcium plage with the estimated average area (in mh) of Big Bear calcium plage.

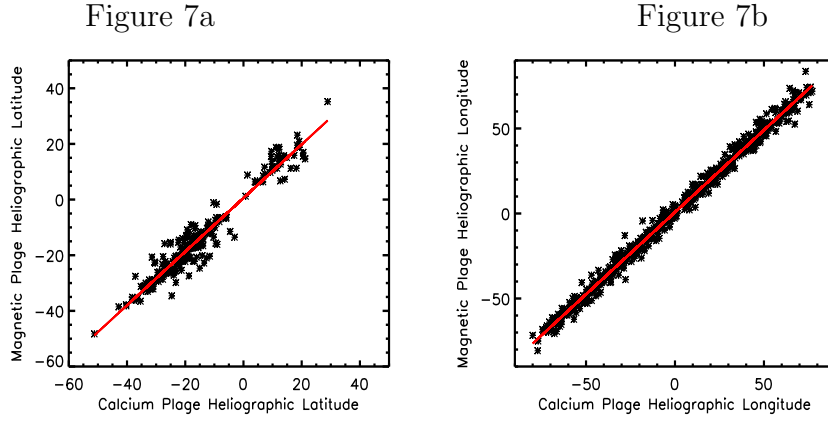


Figure 7: Figure 7a illustrates a scatter plot between estimated average latitude of calcium plage and magnetic plage (detected from the SOHO/MDI magnetograms) latitude. Figure 7b illustrates a scatter plot between average longitude from the central meridian of a detected calcium plage and the magnetic plage.

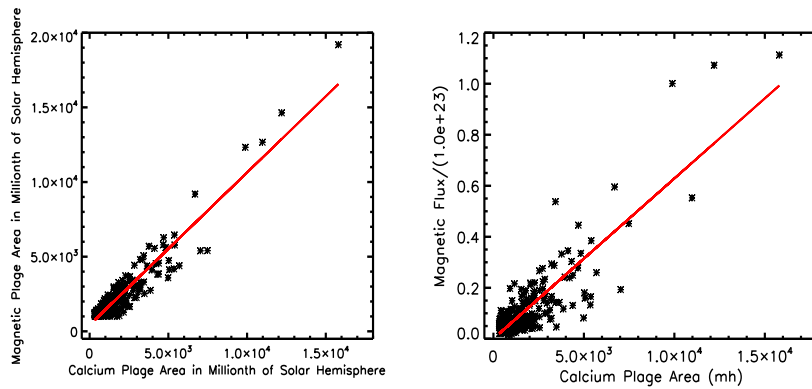


Figure 8: Figure 8a illustrates a scatter plot between estimated average area (in mh) of calcium plage and magnetic plage area. Figure 8b illustrates a scatter plot between average area (in mh) of calcium plage with the magnetic flux (normalized with 10^{23} Mx) of the magnetic plage obtained by SOHO/MDI magnetograms.

2.1.3 Ellipse Fitting

Circle fitting can not be unique and validated unless it should be shown that ellipticity of the image due to atmospheric distortion is negligible. Since we have the detected edge of the solar disk, we can also calculate the ellipticity of the solar disk. For this purpose we employ Halir and Flusser (1998) algorithm which modifies Fitzgibbon and Fisher (1999) algorithm for ellipse fitting. If a and b are equatorial and polar axes, then ellipticity parameter is defined as $|\frac{(b-a)}{b}|$. For the Kodai images, estimated ellipticity parameter for annual and monthly data is presented in Figure 2. One can notice that, as ellipticity ($\sim 0.1\%$ for the yearly average and $\sim 0.1\%$ for the monthly average) of the images is negligible, we are very much safe in fitting the circle to the observed images.

2.1.4 Fixing Heliographic Coordinates

Accurate calculation of heliographic coordinates is necessary, as without accurate computation of the same it is impossible to do any meaningful science with calcium images. Before determining the weighted average heliographic coordinates of detected plages, heliographic coordinates need to be calculated and assigned for all the pixels of the image. Following Smith and Zwart (1990), we compute the heliographic coordinates of each pixel with in the detected calcium image as follows. With daily known values of heliographic latitude (B_0) and longitude (L_0) of the disk center as well as the polar angle P , heliographic longitude L and longitude difference from central meridian l of each pixel are computed.

If $T = (JD - 2415020)/36525$ (JD is the Julian Date of observation and T is the number of Julian centuries since epoch 1900 Jan 0.5), then geometric mean latitude L' , mean anomaly g and right ascension Ω of the ascending node of the Sun are

$$L' = 279.69668^\circ + 36000.76892^\circ T + 0.0003025^\circ T^2, \quad (23)$$

$$g = 358.47583^\circ + 35999.04975^\circ T - 0.00015^\circ T^2 - 0.0000033^\circ T^3, \quad (24)$$

and

$$\Omega = 259.18^\circ - 1934.142^\circ T. \quad (25)$$

Summation of mean latitude L' and C yields the true longitude λ_\odot of the Sun

$$\lambda_\odot = L' + C, \quad (26)$$

here C is equation of the center and is defined as follows

$$C = C_1 + C_2 + C_3, \quad (27)$$

where

$$C_1 = (1.91946^\circ - 0.004789^\circ T - 0.000014^\circ T^2) \sin(g), \quad (28)$$

$$C_2 = (0.020094^\circ - 0.0001^\circ T) \sin(2g), \quad (29)$$

and $C_3 = 0.000293^\circ \sin(3g)$ respectively.

With true longitude λ_{\odot} and corrections for aberration and nutation, apparent longitude λ_a of the sun is computed as follows

$$\lambda_a = \lambda_{\odot} - 0.00569^{\circ} - 0.00479^{\circ} \sin(\Omega). \quad (30)$$

Further parameter ϕ , as given in the following equation, is required for the computation of actual physical ephemeris

$$\phi = \frac{360}{25.38}(JD - 2398220). \quad (31)$$

With inclination ($I = 7.25^{\circ}$) of sun's axis relative to the ecliptic plane, the longitude of the ascending node of the solar equator, K , is given as follows

$$K = 74.3646^{\circ} + 1.395833^{\circ}T. \quad (32)$$

where X and Y are

$$\tan X = -\cos(\lambda_a) \tan(\epsilon), \quad (33)$$

and

$$\tan Y = -\cos(\lambda_{\odot} - K) \tan(I), \quad (34)$$

here λ_a is the sun's apparent longitude corrected for nutation and ϵ is the obliquity of the ecliptic. Then mean obliquity ϵ_0 is computed as follows

$$\epsilon_0 = 23.452295^{\circ} - 0.0130125^{\circ}T - 0.00000164^{\circ}T^2 + 0.000000593^{\circ}T^3. \quad (35)$$

With a correction for nutation, mean obliquity ϵ is given as follows

$$\epsilon = \epsilon_0 + 0.00256 \cos(\Omega). \quad (36)$$

Ultimately daily central coordinates B_0 and L_0 and the polar angle P of the sun are computed as follows

$$P = X + Y, \quad (37)$$

$$B_0 = \sin^{-1}[\sin(\lambda_{\odot} - K) \sin(I)], \quad (38)$$

$$L_0 = \tan^{-1}\left[\frac{\sin(K - \lambda_{\odot}) \cos(I)}{-\cos(K - \lambda_{\odot})}\right] + M, \quad (39)$$

where $M = 360 - \phi$. In this case ϕ varies from $0^{\circ} - 360^{\circ}$ which can be obtained by subtracting integral multiples of 360° .

Owing to daily orbital changes of the Earth around the sun, resolution of pixels also changes. Hence, due to this daily orbital variations, distance R' (in AU) of the Earth from the sun also changes and is given as follows

$$R' = 1.00014 - 0.01671 \cos(g) - 0.00014 \cos(2g). \quad (40)$$

The semi-diameter Rad (in arc-seconds) is given as follows

$$Rad = \left(\frac{0.2666}{R'}\right)^o \times 3600'' . \quad (41)$$

Finally computation of heliographic coordinates is achieved through transformation from sun's image in Cartesian coordinates to the polar coordinates (r, θ') . Mathematical determination of the heliographic coordinates is based on the polar coordinates (r, θ') . For this purpose one has to compute the angular distance ρ of any pixel from the center of the solar disk in the following way

$$\sin\rho = \frac{r}{R}, \quad (42)$$

where R is the radius of the solar disc, as described above in section 2.1.2, estimated by the circle fitting. Next step is to compute heliographic latitude θ and longitude l from the central meridian of any pixel as follows

$$\sin\theta = \cos\rho\sin B_0 + \sin\rho\cos B_0\sin\theta', \quad (43)$$

and

$$\sin l = \frac{\cos\theta'\sin\rho}{\cos\theta}. \quad (44)$$

In order to have accurate estimation of heliographic coordinates, correction for distortion of the projected image due to the telescope also has to be taken into account. For this purpose projected image can be corrected in the following steps

$$T = Rad/15 \quad (45)$$

$$R_0 = \frac{Rad}{(7 \times 36)} \times 10^{-12} \times 29.5953 \cos\left[\frac{\cos^{-1}(-0.00629T)}{3} + 240\right], \quad (46)$$

$$\rho' = R_0 \times \frac{r}{R}, \quad (47)$$

and

$$\rho = \sin^{-1}\left(\frac{\sin(\rho')}{\sin(R_0)}\right) - \rho'. \quad (48)$$

This ρ is then taken as the corrected angular distance and then the heliographic coordinates are computed as mentioned above.

Final step is to estimate the heliographic longitude L by adding longitudinal difference l of any pixel from the central meridian to the value of L_0 such that

$$L = L_0 + l. \quad (49)$$

Table 1: Heliographic coordinates of typical detected calcium plages from the Kodai image

Date of Observation	Lat (Deg)	Err (Deg)	Long (Deg)	Err (Deg)	Corrected Area (mh)
1990 1 1.12	-28.65	0.15	-52.87	0.32	1060.93
1990 1 1.12	-28.01	0.02	58.95	0.034	5706.50
1990 1 1.12	-19.92	0.02	34.03	0.02	588.70
1990 1 1.12	-19.56	0.01	18.73	0.04	3298.71
1990 1 1.12	-11.73	0.03	59.85	0.04	300.57
1990 1 1.12	-14.41	0.02	49.55	0.025	2289.96
1990 1 1.12	-11.58	0.03	36.25	0.02	2355.40
1990 1 1.12	11.53	0.02	-28.93	0.03	601.20
1990 1 1.12	12.44	0.01	4.87	0.05	336.26
1990 1 1.12	14.10	0.02	-45.80	0.03	1727.19
1990 1 1.12	14.59	0.02	14.63	0.04	419.23
1990 1 1.12	24.60	0.02	35.43	0.04	1413.40

2.1.5 Morphological Operations For Plage Detection

Morphological operations are required for detection of plages as they ensure accuracy of the average heliographic coordinates and the area of detected plages. Bilateral filtering is performed before a copy of the spectroheliogram is run through OpenCV's findContours function. This operation is similar to Gaussian filtering such that the image histogram is smoothed, but in Bilateral filtering edges are not smoothed. This allows for detected plages to have similar pixel intensities, but ensures that plage intensities are not redistributed into the background quiescent area of the sun.

Above step is followed by thresholding, which converts the image into a two level colour image. A value for threshold is provided, and all pixel values above this value are converted to 255 (black) while all pixel values below the threshold are converted to 0 (white). The threshold itself is calculated by calculating the median and standard deviation of all pixels lying inside the solar disk for each image. The final threshold is set to the median plus 3 standard deviations. We also tried with a threshold of mean plus 3 standard deviation. In the following we find that both the thresholds yield same results. In Figure 3a we illustrate the original calcium image and in Figure 3b detected plages in the same image is illustrated.

Other morphological operations such as opening (erosion followed by dilation) were also considered, but were avoided since they often split one detected plage into two detected plages. This happened in particular for large plages connected by thin tendrils.

2.1.6 Computation Of Average Heliographic Coordinates

Following Hiremath and Hegde (2013), weighted positional coordinates (heliographic latitude θ_{plage} and the longitude from the central meridian l_{plage}) with their error bars ($\delta\theta$ and δl) are computed as follows. If intensity I_n is n-th pixel of the detected plage, positional coordinates of the plage are the weighted averages which are estimated in the following way

$$\theta_{plage} = \frac{\sum_n \theta_n I_n}{\sum_n I_n} \quad (50)$$

and

$$l_{plage} = \frac{\sum_n l_n I_n}{\sum_n I_n} \quad (51)$$

Similarly errors $\delta\theta$ and δl in the in the positional coordinates are obtained as follows

$$\delta\theta = \frac{\sigma_\theta}{\sqrt{(N)}}, \quad (52)$$

and

$$\delta l = \frac{\sigma_l}{\sqrt{(N)}}. \quad (53)$$

Where σ_θ and σ_l represent, with in each detected plage, standard deviations of latitude and longitude from the central meridian and N is the total number of pixels in the detected plage. Using these formulae, the heliographic coordinates and their errors for each plage in every image are estimated.

For the authentication of our detected plages and their estimation of average positional coordinates, we assume that well developed calcium plages are extension of sunspot flux tubes in the chromosphere. Plage heliographic coordinates are then compared with the heliographic coordinates of the sunspots (in this case we consider Greenwich sunspot heliographic coordinates data) at the photospheric level. In case the observed timings of sunspots are different compared to the observed timings of the Kodai detected plages, we also account for change in the longitudinal difference of sunspots due to rotation of the sun as follows

$$l = l_0 + \Omega\delta t, \quad (54)$$

and

$$\Omega = \Omega_0 - \Omega_1 \sin^2\theta, \quad (55)$$

where δt is the difference of the time of observations, l is the weighted average longitude difference from central meridian, corrected for difference in observation time of sunspot and plage, l_0 is the calculated weighted average longitude difference, Ω is the rotation rate of the sun and, θ is the weighted average heliographic latitude for the plage. In the above equation, Ω_0 and Ω_1 are the constant coefficients that are due to equatorial and high latitude rotation rate of the sunspots. Essentially, this formula accounts for differential rotation rate of the sun.

2.1.7 Projected And Corrected Plage Areas

For area estimation, we use the OpenCV function `contourArea`, which determines the area of each contour in pixels. Since our detected contours are plages, this represents plage area in pixels. By knowing resolution (incase of Kodai Ca II image it is 0.85") of the image, area of each pixel is computed and total area of plage is a sum of area of all the pixels within the detected plage boundary. This area is converted to millionths of solar hemisphere area using the uniquely estimated solar radius. As the sun is a sphere, plages that occur near the solar edges and high latitudes require correction for the projectional effects which is given as follows

$$A = \frac{A'}{\cos\delta}, \quad (56)$$

where A' is projected area and $\cos\delta = \sin B_0 \sin\theta + \cos B_0 \cos\theta \cos l$, with estimated average positional coordinates (θ and l) and B_0 is the heliographic latitude of center of the solar disk at the time of observation.

3 Results

In order to authenticate the estimated positional coordinates and the areas of detected calcium plages, we have following three comparisons: i) photospheric sunspots positional coordinates with the positional coordinates of the chromospheric calcium plages, ii) Kodai calcium positional coordinates and area with the Big-Bear calcium positional coordinates and the area and, iii) positional coordinates and area of the chromospheric magnetic plages (extracted from SOHO/MDI magnetograms) with the positional coordinates and area of Kodai calcium plages,

3.1 Comparison Of Positional Coordinates Of Chromospheric Plages With Sunspot Positional Coordinates

As there is a one-to-one correspondence (Ortiz and Rast 2005, Sivaraman and Livingston 1982) between calcium plages and sunspots, we compare the calculated average positional coordinates (θ and l) of plages detected between 1909 and 2007 with Greenwich sunspot data (<https://solarscience.msfc.nasa.gov/greenwch.shtml>). We find that for observations taken on the same date the heliographic latitudes match very well within a limit of one degree. The calculated heliographic longitude difference from central meridian also matches with the longitude difference of the sunspots within a limit of one degree. These results are illustrated in Figures 4a and 4b respectively. Best way of comparison and authentication is to compare the heliographic coordinates and the area of Kodai calcium plages with the heliographic coordinates and area of calcium plages estimated from other studies. For this purpose, Big Bear Observatory calcium plages are compared (Figures 5 and 6). We find that estimated heliographic coordinates and corrected area (in millionth of hemisphere) of Kodai calcium plages match very well with the Big Bear Observatory

estimated heliographic coordinates and corrected area respectively that clearly authenticates our method of detection and estimation of position and area of calcium plages.

For the year 1990, in the month of Jan, estimated average heliographic coordinates and the corrected area of typical plages are presented in Table 1. The first column represents, year, month and date of observation (in decimal). Second and third columns are the estimated latitude and its error. Similarly fourth and fifth columns are estimated longitude from the central meridian and its error. Whereas the last column represents the corrected area of the plage.

3.2 Comparison Of Positional Coordinates And Area Of Calcium Plages With Positional Coordinates And Area Of Chromospheric Magnetic Plages

It is well established fact that, compared to sunspots, plages decay slowly. Hence, there is every possibility that at least in some cases, sunspots positions may not match very well with the calcium plages. Hence, best way is to compare positional coordinates and the area of calcium plages with the positional coordinates and the area of chromospheric magnetic plages as these activity regions originate near the same region of chromosphere. For such comparison, SOHO/MDI magnetograms are ideally best suited. This is due to the fact that the observed Ni I 6768 Å line (Scherrer *et.al.* 1995) used for generating the SOHO/MDI magnetograms occurs (Jones 1989, Meunier 1999) at about 200 Kms above the photosphere, very near the Ca II line height formation (see Figure 2 of Yang *et.al.* 2009 and, Table 1 of Anusha and Nagendra (2013)). In order to achieve this aim, we use 96 min averaged SOHO magnetograms, a similar method (as described in the above section 2) is used to detect magnetic plages, fix the heliographic coordinates and estimate the area. By using magnetic field intensity of 30 G (two times noise level in the magnetogram; this threshold is to detect correct boundary of the magnetic plage and not the extended diffuse structure) as threshold, we detect magnetic plages. Heliographic coordinates and areas of detected magnetic and calcium plages are illustrated in Figures 7 and 8a respectively. As for the area of detected magnetic plages, although there are positive and negative magnetic flux values, negative flux value pixels are converted into absolute (positive) values and their areas are added to the areas of the positive flux pixels. It is interesting to note that heliographic coordinates and area of calcium plages match very well with the heliographic coordinates and area of magnetic plages authenticating our method of detection and estimation of position and areas of calcium plages.

As described in the introduction, our one of main aims is to investigate long-term (~ 100 yrs) variation of solar magnetic activity. From this study we find that, as there is one to one correspondence between the position and heliographic coordinates, calcium plage area can be used as a magnetic proxy. That means if one finds a relationship between area of calcium plage and magnetic flux of the magnetic plages, nearly 100 years of Kodai calcium area data can be used to investigate the long-term variation of solar magnetic activity. For this purpose, within a detected magnetic plage boundary, negative magnetic flux are converted into absolute (positive) flux values and are added with rest of the positive flux

values in order to estimate the total magnetic flux. A relationship between calcium plage area and magnetic plage total flux is illustrated as a scatter plot in Figure 8b.

4 Conclusions

A code is developed in Python to analyze Kodaikanal Ca II K spectroheliograms. For determination of center and radius of solar disk uniquely, a circle is least square fitted to the detected edge of the solar disk. Further, we find that the Kodaikanal Ca II K Spectroheliograms have a mean ellipticity of 0.0010, which suggests application of circle fitting is reasonable for the Kodai Ca II K spectroheliograms. By using standard astronomical ephemerides, for each pixel of the solar disc, heliographic coordinates such as latitude and longitude are computed. By applying image processing techniques, plages of the chromosphere are detected. This process is optimized using parallel programming. Weighted average heliographic coordinates and area of the plages are computed. From two methods, heliographic coordinates and area of the calcium plages are compared with heliographic coordinates of sunspots and magnetic plages that shows a one to one correspondence and validating our method of detection of Kodai calcium plages.

Acknowledgments

SOHO is a project of international cooperation between ESA and NASA.

REFERENCES

- Alfvén, H. 1943, Arkiv f. Mat., Astron. o. Fys., 29A (12), p. 1-17
- Anusha, L. S. and Nagendra, K. N. 2013, ApJ, 767, 108
- Balmaceda, L. A, Solanki, S. K, Krivova, N. A, and Foster, S. 2009, Journal of Geophysical Research: Space Physics 114, A7
- Barata, T., Carvalho, S., Dorotovi, I., Pinheiro, F. J. G., Garcia, A., Fernandes, J & Loureno, A. M., Astronomy and Computing, 2018, 24, 70
- Bertello, L., Ulrich, R. K., and Boyden, J. E.: 2010, Solar phys, 264, 31
- Bertello, L.; Pevtsov, A. A.; Tlatov, A. G., in Proceedings of a Meeting held at the University of Coimbra, Edited by Ivan Dorotovic, Catherine E. Fischer, and Manuela Temmer. ASP Conference Series, Vol. 504. 2016a, p.213
- Bertello, L., Pevtsov, A. A., Tlatov, A & Singh, J., 2016b, Solar phys, 291, 2967
- Butler, C. J., in IAU 176, 1995, Edited by Klaus G. Strassmeier and Jeffrey L. Linsky, Kluwer Academic Publishers, Dordrecht, p.423
- Chatterjee, S, Banerjee, D and Ravindra, B. 2016, ApJ, 7, 87
- Chatzistergos, T., 2017, Ph.D thesis, University of Gottingen
- Chatzistergos, Theodosios, Ermolli, Ilaria; Solanki, Sami K.; Krivova, Natalie A., 2018, Astron Astrophys, 609, 92
- Ermolli, I, Marchei, E, Centrone, M, Criscuoli, S, Giorgi, F and Perna, C.: 2009a, Astron

Astrophys, 499, 627

Ermolli, I, Solanki, S. K, Tlatov, A. G, Krivova, N. A, Ulrich, R. K and Singh, J. 2009b, ApJ, 698, 1000

Foukal, P., 1996, GRL, 23, 2169

Frasca, A., Freire Ferrero, R., Marilli, E., Catalano, S, et.al., 2000, Astron Astrophys, 364, 179

Frasca, A., K. Biazzo, K., Ta, G., Evren, S and A. C. Lanzafame, A. C, 2008, Astron Astrophys. 479, 557

Frasca, A., Biazzo, K., . Kvri, E. Marilli and . akrl, 2010, Astron Astrophys, 518, A48 A. Fitzgibbon, M. Pulu, and R. B. Fisher. Direct least square fitting of ellipses. 1999, IEEE Transactions on Pattern Analysis and Machine Intelligence, 21(5), 476

R. Halir and J. Flusser. Numerically stable direct least squares fitting of ellipses. In Proc. of Sixth Intl Conf. 1998, Computer Graphics and Visualization, 1, 125

Gokhale, M. H, Javaraiah, J and Hiremath, K. M. 1990, IAU symp, 138, 375

Hiremath, K. M. 1994, Ph.D thesis, Bangalore University, India

Hiremath, K. M. and Gokhale, M. H. 1995, ApJ, 448, 437

Hiremath, K. M. 2009, Sun and Geosphere, 4, 16

Hiremath, K, M. 2010, Sun and Geosphere, 5, 17

Hiremath, K. M an Hegde, M. 2013, ApJ, 763, 1371

Hiremath, K. M. 2015, New Astronomy, 35, 8

Jones, H. P. 1989, Solar phys, 120, 211

Loukitcheva, M., Solanki, S. K. and White, S. M., 2009, Astron Astrophys, 497, 273

Meunier, N. 1999, ApJ, 527, 967

Rodono, M, Byrne, P. B, Neff, J. E, Linsky, J. L, Simon, T, Butler, C. J, Catalano, S, Cutispoto, G, Doyle, J. G, Andrews, A. D and Gibson, D. M., 1987, Astron Astrophys, 176, 267

Smith, P. R and Zwart, J. 1990, in Practical Astronomy with your calculator, Cambridge University Pres

Ortiz, A and Rast, M, 2005, Memorie della Societ Astronomica Italiana, 76, 1018.

Pevtsov, A.A., Virtanen, I., Mursula, K., Tlatov, A., Bertello, L.: 2016, Astron Astrophys, 585, A40.

Priyal, M, Singh, J, Ravindra, B, Priya, T. G and Amareswari, K. 2014, Solar phys, 289, 137

Priyal, M, Singh, J, Ravindra, B and Rathina, S. K. 2017, Solar phys, 292, 85

Scherrer, P. H, Bogart, R. S, Bush, R. I, Hoeksema, J. T, Kosovichev, A. G, Schou, J, Rosenberg, W, Springer, L, Tarbell, T, D, Title, A. Wolfson, C. J, Zayer, I and MDI Engineering Team, 1995, Solar phys, 162, 129

Sivaraman, K. R. and Livingston, W. C. 1982, Solar phys, 80, 227

Tlatov, A. G, Pevtsov, A. A and Singh, J. 2009, Solar phys, 255, 239

Yang, S. H. and Zhang, J. and Jin, C. L. and Li, L. P. and Duan, H. Y. 2009, Astron
Astrophys, 501, 745